Numerical and experimental crossed analysis of coated nanostructures through nanoindentation

Vincent Fauvel [1,2], Yves Gaillard*[1], Raphaël Guillemet [2], Patrick Garabédian [2], Fabrice Richard [1]

[1] Université Bourgogne Franche-Comté, Institut FEMTO-ST, CNRS/UFC/ENSMM/UTBM, Département Mécanique Appliquée, 24 rue de l'Épitaphe, 25000 Besançon, France

[2] THALES Research & Technology, 1 avenue Augustin Fresnel, 91120 Palaiseau, France

Graphical abstract

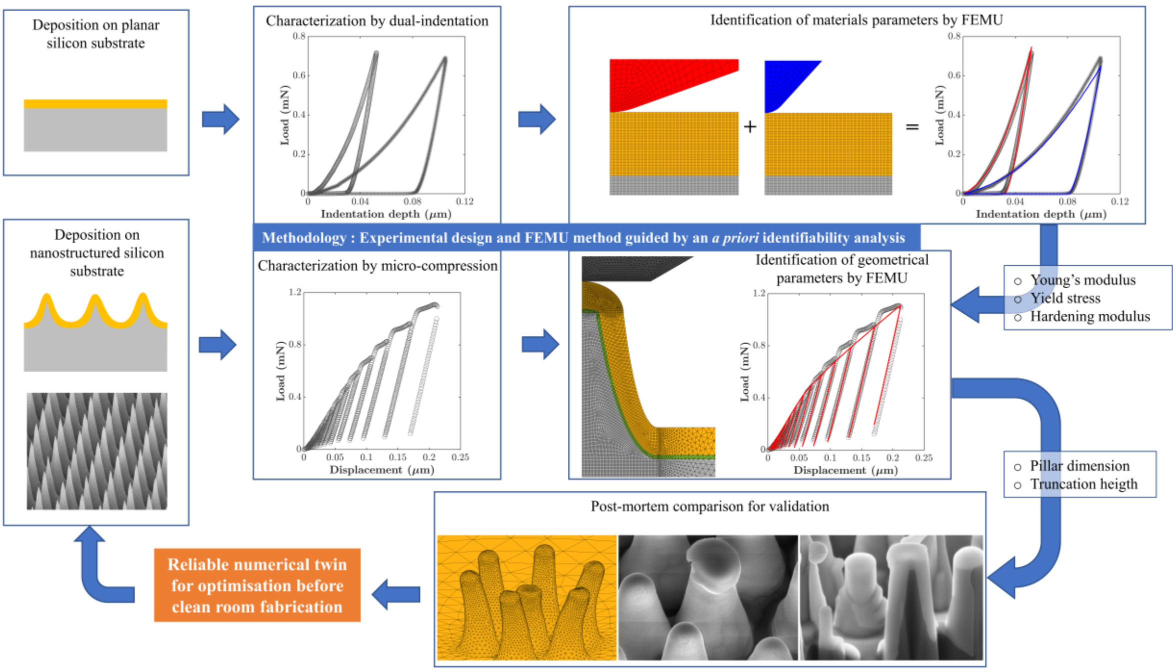

Abstract

Nanostructuration can bring unique functional properties to optical window surfaces, such as superhydrophobic and antireflective capacities. However, their sustainability is conditioned by the mechanical resistance of the nanostructures, which can exhibit high aspect ratios to meet the military industry requirements in terms of optical transmission. Thus, improving the mechanical strength of such surfaces without affecting their functional properties is a key challenge. In that respect, this work investigates the protective impact of an annealed alumina thin film on a nanostructured silicon surface with conical shape. First, the elasto-plastic properties (Young's modulus, yield stress and hardening modulus) of the untreated and heat-treated coating are extracted from nanoindentation experiments on a plane sample using a numerical approach. The latter relies on the finite element model updating method from a 2D axisymmetric finite element model of a dual nanoindentation test, combing Berkovich and cube corner geometries, designed by a methodology based on an *a priori* identifiability analysis using an indicator (I-index) to ensure a good conditioning of the inverse problem. Identification results reveal that the heat-treated coating is stiffer and harder, which is in accordance with the crystallisation phenomena highlighted by X-ray diffraction measurements. Thereafter, single nanostructure microcompression tests are implemented, and the obtained mechanical responses clearly illustrate the protective effect of the coating and emphasise different solicitation regimes. Simulations of microcompression tests using 2D axisymmetric and 3D finite element models which integrate the previously identified parameters on plane sample allow to corroborate some of the experimental observations. Lastly, two uncertain and yet essential nanostructure geometric parameters for accurate simulations, are retrieved using the numerical methodology applied on plane sample and validated by comparing identified values with post-mortem microscopic observation of a tested nanocone. It is thus shown that well-designed nanoindentation experiments, using *a priori* identifiability analysis, allow to identify with confidence reliable constitutive material parameters which can be used to describe the mechanical behaviour of a coated nanostructure. This methodology undeniably simplifies the design and optimization of coated nanostructures by avoiding too many unnecessary cleanroom manufacturing steps.

Keywords: Nanoindentation, Microcompression, Nanostructures, Inverse analysis, Thin film

1. Introduction

Nanostructuration of surfaces and coatings can confer impressive physical properties to materials for various applications in search for efficiency and innovative functionality, such as gas self-transportation [1], passive or active smart functionalization [2], sensing and corrosion inhibition [3] and superhydrophobicity [4–7].

In the scope of optical materials, surface nano-patterning can give remarkable antireflective, superhydrophobic, self-cleaning and antifogging properties to optical windows by mimicking behaviours and properties that nature provides [8–12]. Indeed, nanometric-scale rugosity with specific geometry can be found on the surface of some insects. The eyes of some moth species present structures of about 100 nm which minimise the reflexion of their eyes while they are inactive the day, protecting them against predators [13,14]. The wings of some butterfly species also exhibit submicrometric texture conferring high transparency and protection by mimicry [15–18]. Cicada wings with similar rugosity are also known to show antifogging and self-cleaning capabilities [8,9,19,20].

Inspired by these natural surfaces, nanostructures with different shapes (pillar, cone) can be fabricated and bring both antireflection and superhydrophobic properties making them particularly interesting for multifunctional optical systems [21–27]. However, these two characteristics are generally met for nanopillars of conical shape with very high shape ratio [9,19,28–30]. However the sustainability of these nanostructured surfaces and their properties is conditioned to a key aspect: their mechanical resistance [31], as such optical systems may be subjected to harsh environment in defence applications like sand and rain erosion. The few existing studies covering the mechanical resistance of nanostructured materials in harsh environment have reported erosion resistant-capability of hydrophobic surfaces fabricated on the bulk material [32], and the superiority of a direct material structuration compared to antireflective coatings in terms of losses of optical transmission after sand-erosion tests [33,34]. However, these losses are still significant, and associated with visible damage on the surface, which arguably affects the superhydrophobic properties. In fact, these very high aspect ratio structures exhibit generally a very brittle behaviour and increasing their mechanical resistance without overly affecting their optical and hydrophobic properties is a crucial issue.

Among the different solutions, the deposition of a thin protective film constitutes a serious track to protect optical materials [35,36]. The alternative studied in this work is essentially based on a patent of invention which relates the uniform and conform deposition of an alumina thin film by Atomic Layer Deposition on a silicon nanostructured optical window with high aspect ratio and exhibiting superhydrophobic and antireflective functions [37]. The choice of an alumina coating is justified by its propensity to crystallize and harden with high temperature heat treatments. This technical response however opens the way to new questioning. The first one is the need to use a numerical optimisation process, through a numerical twin, to lead to an optimal shape of the nanostructure, an optimal lattice (grid), and an optimal film thickness, because such optimisation by round trips in clean room appears to be too much time consuming and expensive. The second concerns the evaluation of the protective power of such kind of coating. If impact test can be experimentally performed [33,34], it seems very difficult to envisage numerically, because of the large variability of such kind of test. In fact, taking into account the calculation time of a single impact test, the impact speed, the shape and nature of the shocking particle appears as so many parameters for which it is unreasonable to cover the whole space of possibilities. Single nanostructure testing may appear more realistic numerically but more complicated experimentally. And finally, would it be possible to find an equivalent mechanical test easier to implement experimentally but also numerically in order to reliably determine the true mechanical properties of such coated nanostructures.

In this paper, hexagonal gridded silicon nanostructures coated with alumina are studied. Nanostructure fabrication but also Atomic Layer Deposition (ALD) process are firstly described. Then, when it comes to determine mechanical properties of coatings and micro or nanostructures, instrumented nanoindentation is generally naturally evoked and required. Indeed, the coating mechanical response is determined when deposited on a planar silicon wafer but also on a nanostructured sample. In order to rely on the different mechanical responses to the constitutive material properties and to the nanostructure geometrical parameters, finite element models of the different tests are built. To use reliable values of the previously cited parameters in different mechanical tests, a robust inverse method is built based on a identifiability index previously presented in [38,39]. The constitutive and morphological parameters estimated, the robustness of this method is finally validated by comparing identified and experimental nanostructure geometry.

2. Materials and method

This section presents the fabrication processes leading to a coated nanostructured silicon optical window with conical pillars and the mechanical probing of the fabricated samples.

2.1. Sample fabrication and characterization

Nanostructuration processes are presented in this subsection, as well as the thin film deposition and its subsequent annealing, and lastly the conditions of microscopic characterization of the fabricated samples.

2.1.1. Nanostructuration

The fabrication of nanostructured surfaces has been achieved on an oriented (100) silicon substrate, which involves two main processes: the definition of the patterns on the substrate by UV-assisted NanoImprint Lithography (UV-NIL), and the selective etching onto the substrate by Inductively Coupled Plasma Reactive Ion Etching (ICP-RIE) to obtain conical structures. As shown on Fig. 1, UV-NIL allows to replicate in one step sub-micrometric patterns (silicon dots) on the silicon substrate surface. In this present work, this process uses specifically the deposition of two commercial resins, and the UV-NIL is applied on the first resin to create the patterns (Fig. 1a). Then, the second resin is opened with an adapted developer as shown on Fig. 1b. Then, ICP-RIE allows to etch with an anisotropic manner the silicon dots to obtain the final conical shape as shown on Fig. 1c.

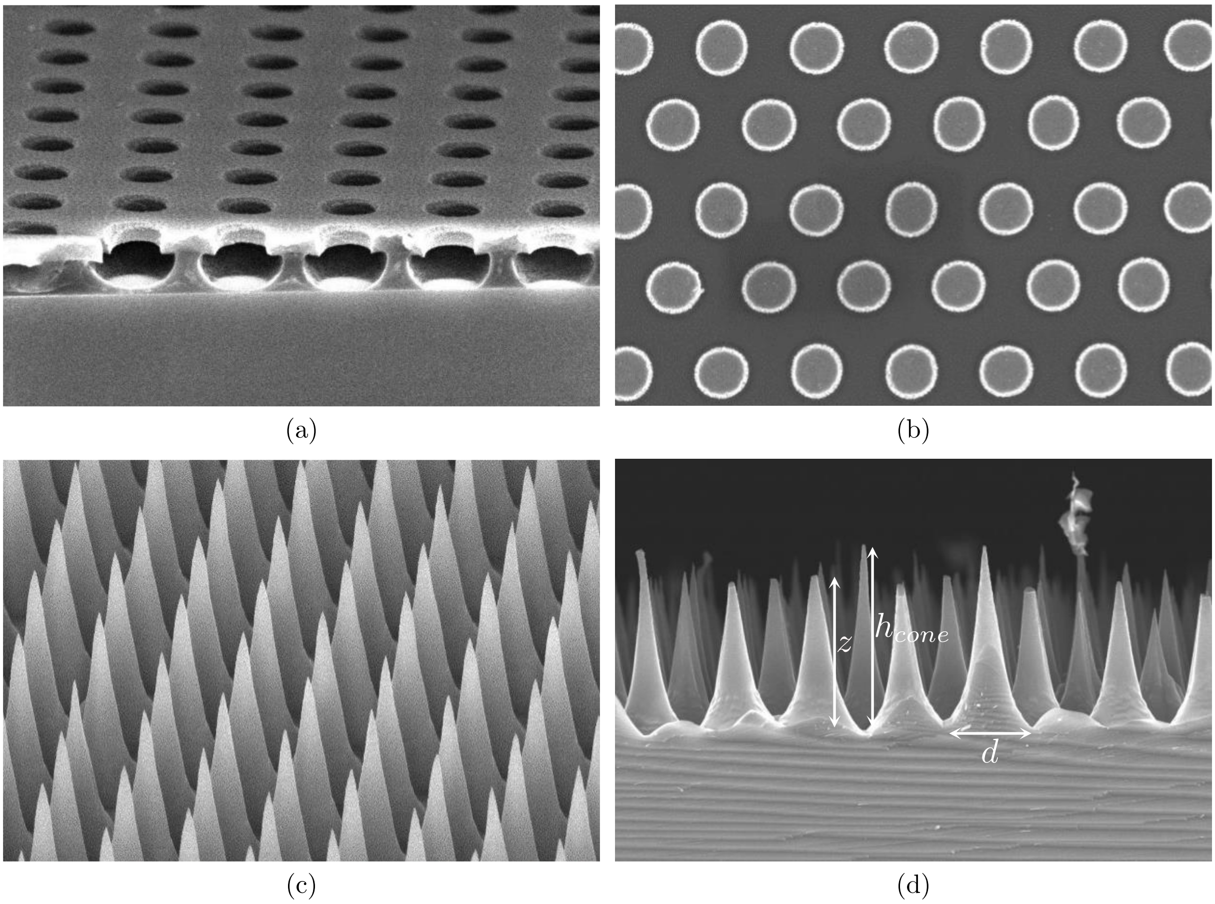

Fig. 1. Scanning Electron Microscope (SEM) images obtain at different steps of fabrication of the nanostructures: (**a**) after the nanoimprint lithography, (**b**) after removing the resin and (**c**) after the selective etching conducted by ICP-RIE. A transversal view of the obtained nano-cones is shown on (**d**). No scale is provided for confidentiality reasons.

Fig. 1d shows a transversal view of the obtained nanostructures. The majority of them exhibit the desired conical shape. Cones appear to be truncated at different heights. Three main parameters are necessary to fully describe the geometry of a single pillar: the distance, d, between two pillars, the height, h_{cone}, of the pillar without any truncation and the altitude, z, of truncation, that also determine the radius, r, of truncation. If the distance d is well known, h_{cone} and above all z are complicated to assess and can be different for each pillar composing the entire surface.

2.1.2. Thin film deposition and annealing

Amorphous alumina (Al_2O_3) thin film has been deposited on nanostructured samples at 200°C by plasma enhanced atomic layer deposition with TriMethylAluminium $Al(CH_3)_3$

(TMA) precursor and O_2 gas with a targeted thickness of 200 nm, confirmed by ellipsometry. Prior to deposition, Si nanostructured substrates have been cleaned into diluted hydrofluoric acid (HF 1:5) to remove the native SiO_2 layer. After the HF cleaning, ellipsometry measurements show that a native oxide layer of around 0.5 nm still remains on the surface. This cleaning procedure is required to avoid the blistering of the alumina coating during the subsequent annealing due to hydrogen degassing trapped in the impure native oxide layer. However, this phenomenon has been observed in several samples, despite HF cleaning, due to the rapid regrowth of the native oxide during sample handling. Furthermore, it also shows that the alumina layer does not sufficiently adhere to the substrate. Thus, the growth of a thermal silica layer formed by oxidation of silicon before Al_2O_3 deposition has been conducted, as it has been shown in literature that this interlayer increases the adherence of alumina coatings on silicon and avoid blistering [40,41]. This layer has been grown by rapid thermal annealing at 1000°C during 3min in O_2 gaseous atmosphere, conditions for which the obtained thickness is estimated around 30 nm by ellipsometry. The surface morphology characterisation of Al_2O_3 film on silicon nanostructures has been performed by Scanning Electron Microscopy (Fig. 2a) and show excellent conformity and large-area uniformity (Fig. 2b). After the deposition process, nanostructured samples have undergone heat treatments (HT) at 900, 1000 and 1100°C during 90 seconds in a neutral N_2 atmosphere. Such deposition and heat treatments has been also realised on silicon substrate without nanostructure. An additional study of the crystallization behaviour of the alumina coating has been conducted by X-ray diffraction and presented in Appendix.

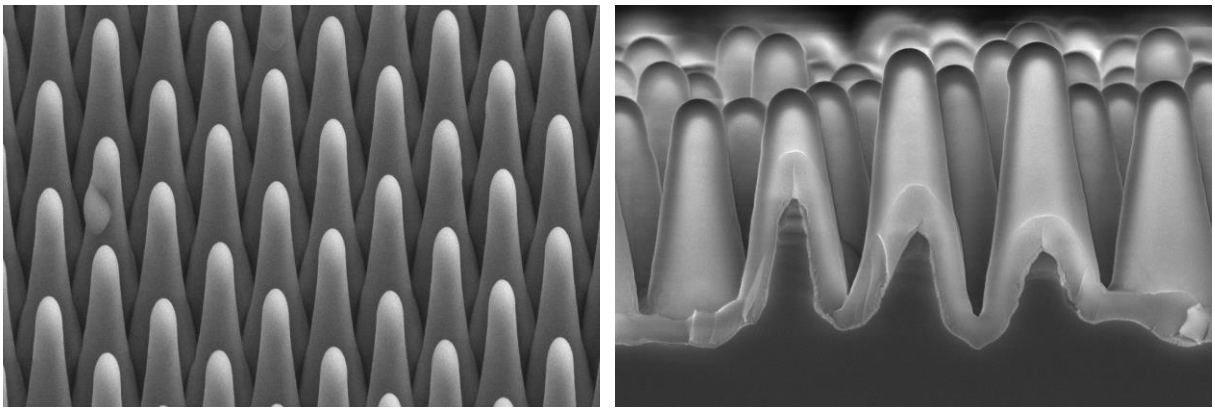

(a) (b)

Fig. 2. SEM images of the nanostructures obtained after the AL_2O_3 deposition. (**a**) Plane view and (**b**) cross sectional view. No scale is provided for confidentiality reasons.

2.1.3. Microscopic characterization

Scanning Electron Microscope (SEM) observations and Focused Ion Beam (FIB) cross sections have been realised on nanostructured samples to obtain experimental *post-mortem* imprints of individual cones. A Zeiss Sigma HD microscope, associated with a FIB column positioned at 54° from the electron column has been used for this purpose.

2.2. Mechanical probing

This subsection presents the experimental conditions of the performed nanoindentation tests, and an analytical analysis method applied on force-displacement ($P-h$) outputs which gives a first estimation of the elastic properties of the coating. Lastly, the microcompression testing on nanostructured sample is detailed.

2.2.1. Nanoindentation tests on plane sample ~~and analytical analysis method~~

Nanoindentation has been performed using an Anton Paar ultra-nanoindenter (UNHT). A Berkovich (B) and a cube corner (CC) tip shapes have been used. Berkovich projected contact area shape function has been calibrated using fused silica. Hardness H_{IT} and apparent elastic modulus E_{app} have been extracted using the Oliver and Pharr method [47] assuming 0.3 Poisson's ratio, written respectively as:

$$H_{IT} = \frac{P_{max}}{A_c}, \tag{1}$$

with P_{max} the maximum indentation depth and A_c the projected contact at maximum load, and:

$$\frac{1}{E_{app}} = \frac{1}{M_c} + \frac{1-\nu_i^2}{E_i} \text{ with } \frac{1}{M_c} = \frac{1-\nu_c^2}{E_c}, \tag{2}$$

where M_c, the equivalent reduced modulus and the physical quantity measured by nanoindentation, drives the elastic contribution of the composite system film+substrate, (E_c, ν_c). The equivalent Young's modulus and Poisson's ratio (E_i, ν_i) are the mechanical properties of the indenter (1141 GPa and 0.07 for diamond).

Berkovich indentations have been performed at a constant $\dot{P}/P$, where P is the force applied on the indenter, superimposing a small sinusoidal signal (Continuous Stiffness Measurement CSM) in order to measure the evolution of the mechanical properties, hardness and elastic modulus, as a function of penetration depth [48,49].

Berkovich and cube corner indentations have been also performed in depth-controlled mode in order to feed the inverse analysis. The full protocol is described elsewhere [50].

2.2.2. Analytical analysis method

In order to firstly evaluate intrinsic elastic modulus of the thin film analytically, a model based on King's and Bec's assumptions [51,52] has been applied on CSM measurements. M_c from equation (2) can be expressed as a function of the elastic properties of the film $M_f(E_f, \nu_f)$ and the substrate $M_s(E_s, \nu_s)$:

$$\frac{1}{M_c} = (1-\phi)\frac{1}{M_f} + \phi\frac{1}{M_s} \text{with } \frac{1}{M_f} = \frac{1-\nu_f^2}{E_f} \text{and } \frac{1}{M_s} = \frac{1-\nu_s^2}{E_s} \tag{3}$$

where ϕ is a function describing the weight of M_s in the evaluation of the composite modulus M_c. ϕ should tend to 1 when the penetration depth h tends to 0, and to 0 when the penetration depth tends to infinity. For this reason, Gao *et al.* [53] used an exponential model which allows to account for the majority of length scale independent experimental cases. ϕ can be written as:

$$\phi = \exp\left[-A\left(\frac{t}{a_c}\right)^B\right] \tag{4}$$

where t is the thickness of the layer and a_c is the equivalent contact radius between the indenter and the sample. A and B can be adjusted numerically to best fit experimental measurements. The means of these parameters remains very complicated as it depends both on the experimental conditions, other material's parameters such as film and substrate yield stress and hardening, and interface conditions between film and substrate.

2.2.3. Microcompression tests on nanostructured sample

The nanostructured surfaces have been indented using a flat-ended conical indenter with a radius of 900 nm in order to probe them individually. Such kind of test are in the following designated as microcompression test. Microcompression tests have been performed on nude and covered nanostructured sample exhibiting the 30 nm thick silica interlayer.

3. Numerical analysis method

This section concerns the presentation of the finite element models used to simulate the mechanical response of coated planar and nanostructured substrates solicited respectively in nanoindentation and microcompression.

3.1. Finite element modelling

Nanoindentation and microcompression tests have ben modelled using ANSYS Mechanical APDL software. The finite element models used to describe Berkovich and cube corner indentations of samples without nanostructures are described elsewhere [38,50]. For calculation time reasons, two different equivalent 2D axisymmetric models using conical indenters having respectively a 70.3° and 42.3° equivalent half angle have been used. The 2D equivalent conical representation of Berkovich and cube corner indenters are shown in Fig. 3a and b.

The nanostructured samples have been modelled in 2 and 3 dimensions. On Fig. 3c and d, one can appreciate the three geometrical parameters used to described geometrically a single nanocone, namely the distance d between two nanocones, the height h_{cone} of the nanocone before truncation, and r the radius of truncation of the nanocone. The 2D axisymmetric model can be uniquely used to describe the mechanical behaviour of a single nanostructure, the hexagonal structure cannot be described axisymmetrically. This model is intended to be included in a Finite Element Model Updating process, addressed in section 3.3, as well as the 2D model mentioned above used to describe the indentation of samples without nanostructure. The 3D model takes into account the compressed single nanostructure and its first neighbours, *i.e.* six nanostructures distributed along an hexagonal lattice structure.

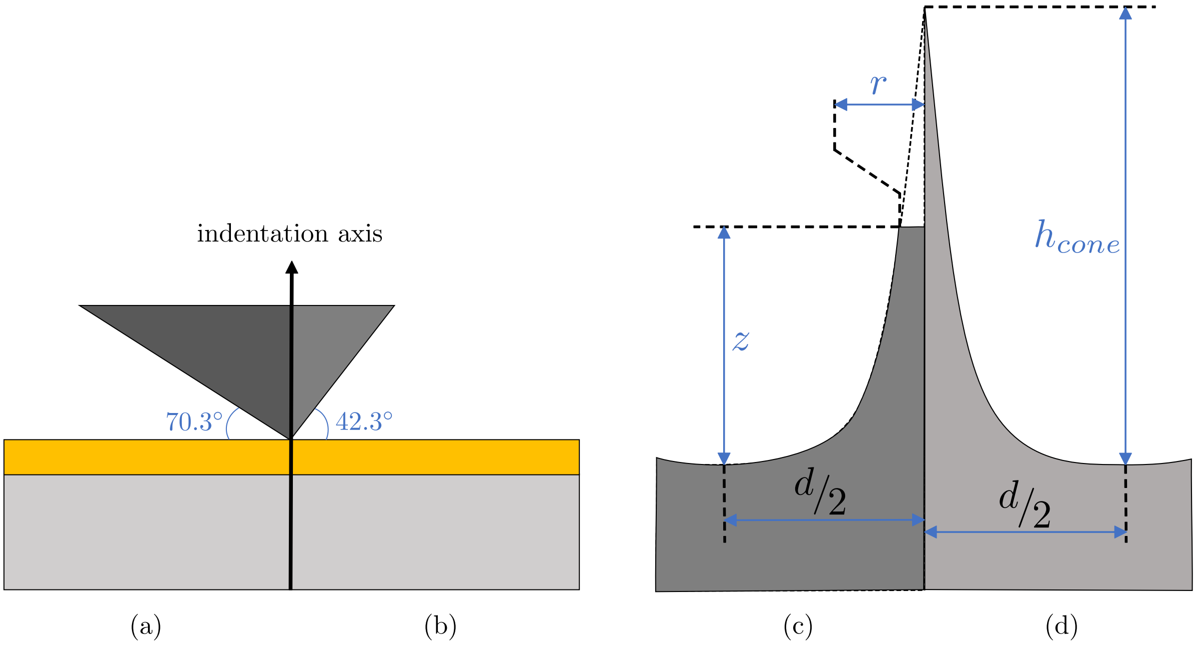

Fig. 3. Schematic illustration of the modelled samples solicited in nanoindentation and microcompression. (**a**) Comparison between a thin film indentation with a Berkovich and (**b**) a cube corner equivalent cone. (**c**) Comparison between a half truncated nanocone and (**d**) a half entire nanocone. h_{cone} is the height of the cone, z the altitude of truncation and r the radius of truncation. d is the distance between two adjacent cones.

Fig. 4 shows the 2D axisymmetric model. Four nodded elements with a linear interpolation have been used to mesh the single coated nanostructure. The substrate, far from the pillar, is modelled with six nodded triangle elements with a quadratic interpolation (PLANE183). The model includes the silicon nanostructure (light grey), the 200 nm alumina layer (yellow), and the 30 nm silica inter-layer (green). The diamond truncated conical indenter (grey) is meshed with six nodded triangle elements with a quadratic interpolation. The typical size of the element just under the contact zone is 10 nm.

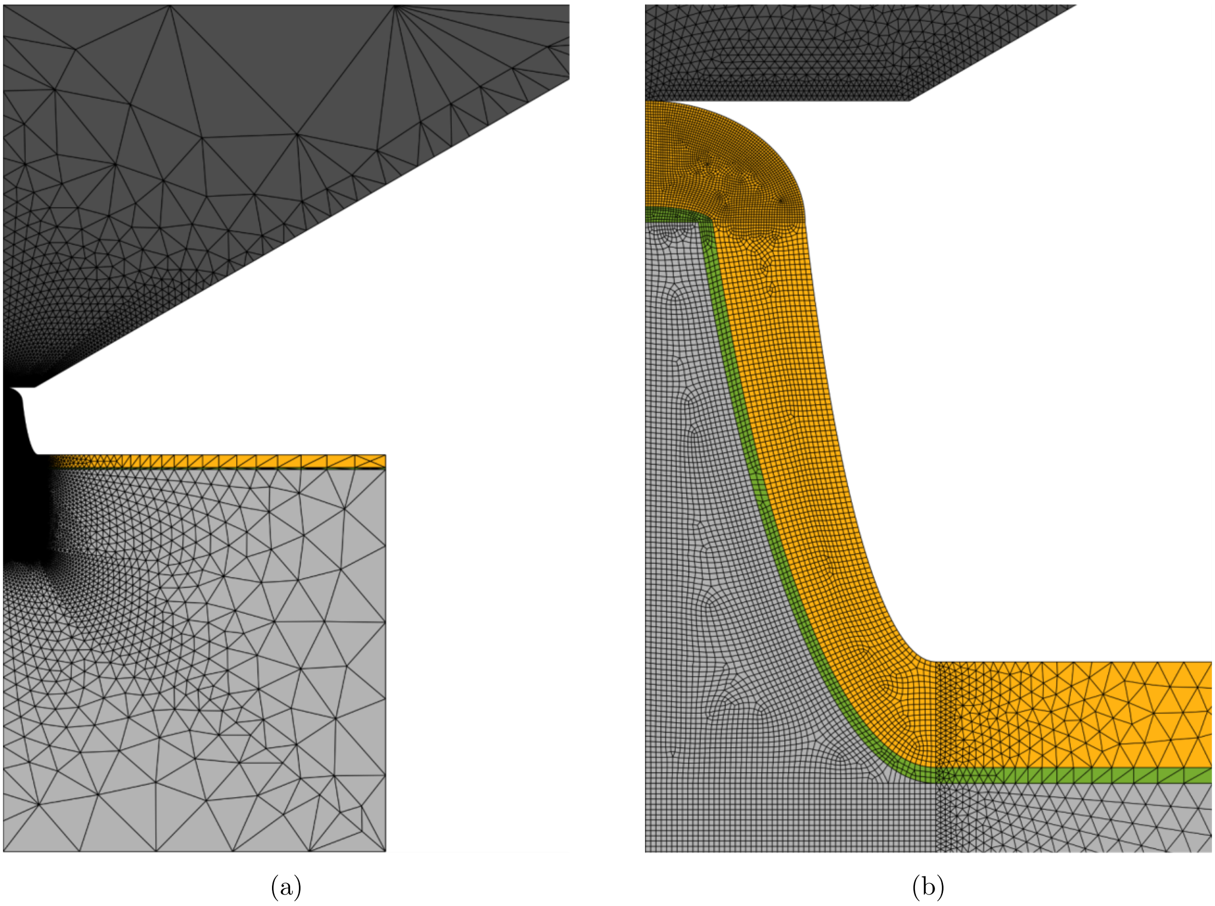

Fig. 4. 2D axisymmetric finite element model of the microcompression of a single nanostructure with a truncated cone. (**a**) Complete model showing the conical indenter and the layered single pillar. (**b**) Magnification of the pillar where the Al_2O_3 film (yellow), the thin oxide layer (green), the substrate (light grey) and the diamond indenter (grey) can be distinguished.

Fig. 5 shows the 3D model presenting the single nanostructure and its six neighbours distributed following a hexagonal structure. Tetragonal elements having 10 nodes and using a quadratic interpolation have been used (SOLID187). This model includes only the silicon nanostructure and the 200 nm alumina layer. The diamond truncated conical indenter is also meshed with the same type of element. This 3D model allows to take into account the tilt between the indenter and the surrounding nanostructures. The typical size of the element just under the contact zone is 30 nm.

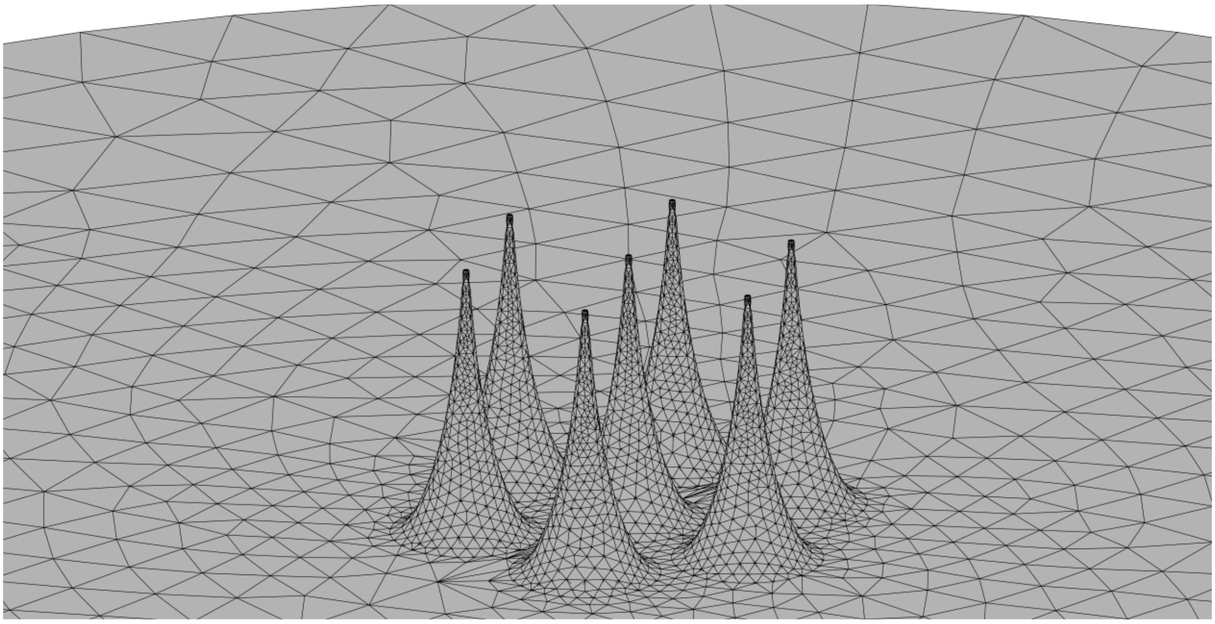

(a)

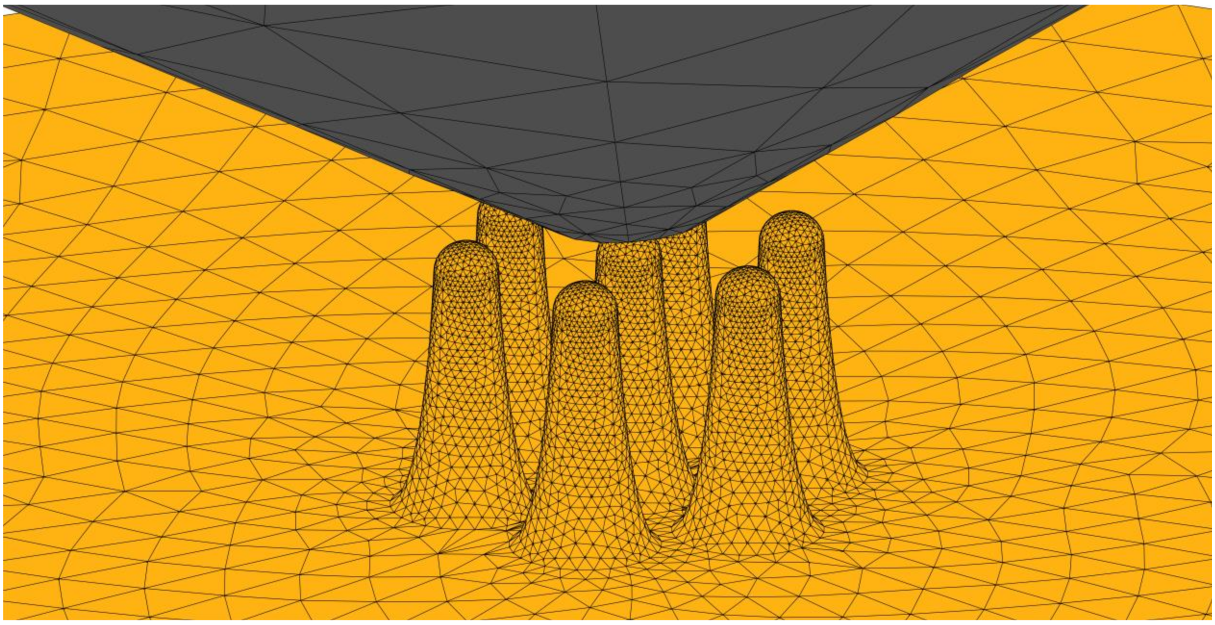

(b)

Fig. 5. 3D finite element model of the microcompression test of a single nanostructure and its first neighbours. (**a**) Mesh of the initial truncated conical silicon nanostructure and (**b**) complete 3D model showing the tilted conical indenter (grey), the protective Al_2O_3 layer (yellow) and the silicon substrate (light grey).

For both model the contact is ensured by an augmented Lagrangian algorithm for normal contact and a penalty algorithm for the tangential contact, called “normal Lagrangian” in ANSYS. A friction coefficient of 0.2 has been used. For both models, all the degrees of freedom of the upper side of the indenter are coupled, and those of all the nodes of the underside are blocked.

3.2. Materials behaviour

The mechanical behaviour of each material constitutive of the composite system film - substrate can be modelled by a bilinear elasto-plastic law. The complete description of this law used in the finite element models can be found in our previous work [38]. In the case of a uniaxial tensile test, the elasto-plastic law can be written as:

$$\sigma = E\varepsilon \qquad \text{for} \quad \sigma < \sigma_y, \tag{5}$$

$$\sigma = \frac{EH}{E+H}\varepsilon \quad \text{for} \quad \sigma \geq \sigma_y \tag{6}$$

where σ is the Cauchy tensile stress and ε is the logarithmic tensile strain. Table 1 summarises the parameters controlling this law.

	E (GPa)	ν	σ_y (GPa)	H (GPa)
Behaviour	Elasticity		Plasticity	
Silicon substrate [54–56]	173	0.21	Id	0 (perfectly plastic)
SiO_2 oxide layer [57]	72	0.17	6.4	0
Al_2O_3 film	Id	0.30	Id	Id
Diamond tip [47]	1141	0.07	∅	

Table 1. Elasto-plastic parameters driving the materials behaviour law in the finite element models. E is the Young's modulus, ν the Poisson's ratio, σ_y the initial yield stress and H is the hardening modulus. "Id" means that the value of this parameters will be determined from the inverse procedure proposed by Fauvel *et al.* [38].

3.3. FEMU method guided by identifiability index

The Finite Element Model Updating (FEMU) method guided by an *a priori* identifiability index (I-index) has been used in order to assess to the unknow values of the mechanical material parameters (E, σ_y and H) of the film. The I-index and its calculation is fully described in [38]. Using a set of plausible parameters, the I-index enables, on one hand, to detect whether the inverse problem is ill-posed before attempting its resolution and, on the other hand, provides guidelines for designing the experiments to be carried out in order to well-posed it. By means of a dimensionless operator based on the numerical sensibility of the $P-h$ curves to material parameters computed with an initial set of plausible parameters, the I-index quantifies the stability of this potential solution and thus the well-posedness of the inverse problem [58]. Roughly, having a I-index inferior to 2 ensures that the identification protocol is robust [59]. The robustness of this methodology has been widely proven in the last ten years and has shown its full potential to identify material parameters of viscoelastic and viscoplastic laws with work hardening in the case of bulk materials [50,60] and thin films [38]. Particularly, for thin film materials, it has been shown that the use of two indenter tips, respectively a Berkovich and a cube corner, can be used to identify with confidence both one elastic and two plastic parameters of the film (I-index=1.9) [38,39]

The FEMU method is based on the calculation of a cost function that characterises the gap between experimental data and numerical simulation. The minimisation of this cost function is ensured by a variant of the Levenberg-Marquardt algorithm implemented in MIC2M software [61].

4. Mechanical properties extracted from planed samples using nanoindentation curves

This section focuses on experiments conducted on planar samples. The elastic modulus and hardness of the coating, before and after heat treatment, are firstly estimated by applying the analytical analysis method presented in section 2.2.1. Thereafter, the use of an inverse analysis of a numerical model of nanoindentation tests have allowed to extract not only the elastic modulus but also the two intrinsic parameters describing the plasticity of the film, according to the bilinear elasto-plastic law presented in section 3.2, *i.e.* the initial yield stress σ_y and the hardening modulus H. Indeed, extracting reliably these intrinsic properties is essential to correctly simulate the mechanical response of coated nanostructures solicited in microcompression.

4.1. Elastic modulus and hardness using analytical method

Fig. 6 present the results obtained by Berkovich instrumented indentation on a silicon substrate and Al_2O_3 thin films having a thickness of 100 nm. The force-displacement curves obtained on a nude and coated substrate are very similar. The evolution of the hardness and elastic modulus given by the CSM method is however more meaningful. During the first stage of penetration, below 50 nm, the measured hardness is clearly lower for the coating than for the silicon. Concerning the elastic modulus, it is not trivial. For penetration depth under 20 nm the modulus of the silicon and the coating are in the same order of magnitude, given the experimental uncertainties. For greater penetration depth the elastic modulus of the coating appears to be always slightly higher than the one of the silicon. This difference appears to be significant and cannot be attributed to the difference of Poisson's ratio as the one of the coating is 0.3 and the one of the substrate is 0.21. Equations (2) and (3) have been used to extract the indentation elastic modulus of the film M_f considering an indentation elastic modulus M_s of 180 GPa for the substrate ($E_s = 173$ GPa$, \nu_s = 0.21$). The result obtained using the analytical model differs from the experimental observation made above as the reduced elastic moduli deduced from equation is 160 GPa for the film, *i.e.* slightly under the one of the substrate. Given the considered thickness of the film, these values are mainly influenced by the first 25 nm of penetration depth. However, it is also in this range of depth that the main experimental uncertainties, like surface roughness and CSM control, are influent. Roughness and uncertainties on the CSM signal conduct to an underestimation of the stiffness of the material [62–64], that could explain the low reduced modulus obtained for the coating. Furthermore, these same effects are those that lead to an underestimation of the indentation elastic modulus of the silicon, deduced also from equations (2) and (3), evaluated at 168 GPa, instead of the classical 180 GPa generally reported and measured for higher depths [65].

Fig. 6 also present the results obtained for the heat-treated sample. Their interpretation is simpler as both hardness and elastic modulus exhibit a clear tendency to decrease with increasing the penetration depth. The values of the extracted indentation modulus, between 258 and 270 GPa following the heat-treatment, are clearly higher than the one of the as-deposited coating. However, there is no clear effect of the temperature as the $P - h$ curves and the evolution of the indentation elastic modulus and the hardness are almost indistinguishable. The heat treatment has a clear hardening and stiffening effect, which is in line with the crystallisation process observed by XRD and evocated in Appendix.

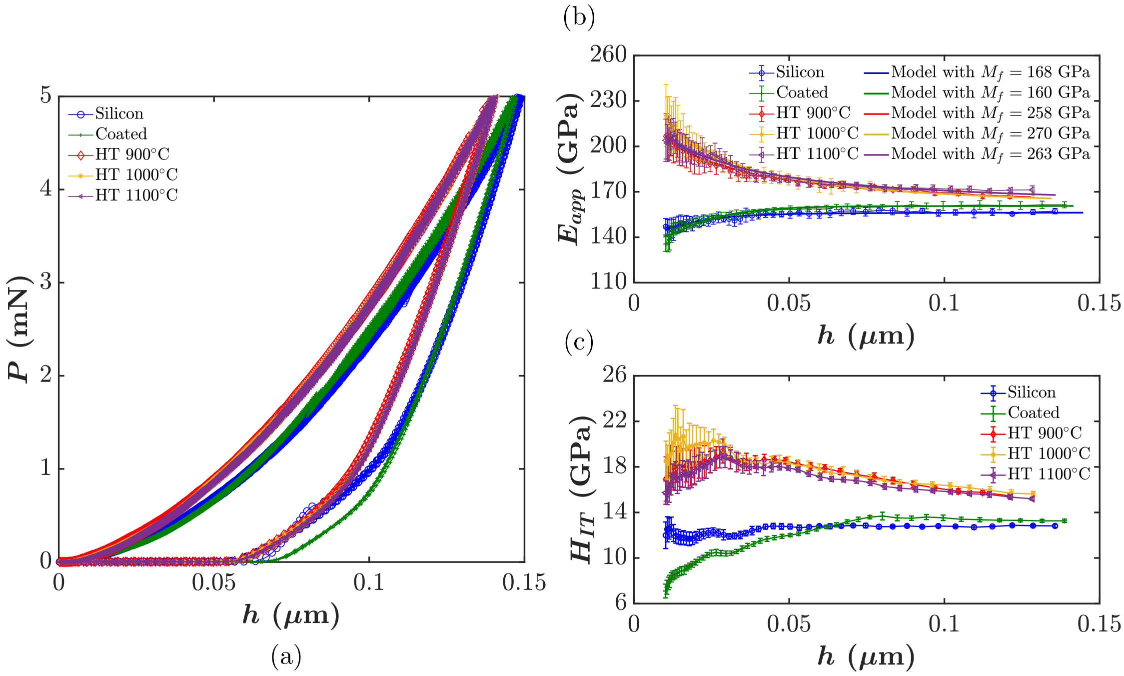

Fig. 6. Experimental responses of Berkovich instrumented indentations on a silicon substrate and 100 nm Al_2O_3 thin films as-coated and annealed at different temperatures. (**a**) Load-displacement curves. (**b**) Apparent elastic modulus E_{app} versus indentation depth h and (**c**) hardness H_{IT} as a function of indentation depth, both obtained using the analytical analysis method presented in section 2.4.1. The plotted curves and associated error bars represent an average of 5 tests for each sample.

4.2. Elastoplastic material properties using FEMU method

An inverse analysis has been performed considering both Berkovich and cube corner indentation responses. The main result of this identification procedure for samples without post-deposition heat treatment is presented in [38]. It is demonstrated that the good way to identify the true mechanical properties of the film shall take into account also the yield stress of the silicon substrate. Thus, four thermomechanical parameters are determined from the Berkovich and cube corner composite responses of the film/substrate system: three for the elastoplasticity of the film (Young modulus E, initial yield stress σ_y and hardening modulus H) and one for the plasticity of the substrate (initial yield stress σ_{ys}). This procedure is repeated for the heat-treated samples. The results are shown in Fig. 7 and summarized in Table 2. Experimental and simulated $P-h$ curves exhibit a good adequation. Associated with an identifiability index of 2, the identification procedure can be considered as robust. Indeed, analysing the values given in Table 2, the following results can be underlined. First, the elastic modulus of the coating before HT is slightly higher than the one of the substrate as suspected in the previous part. Secondly, as hoped, the heat treatment leads to a significant increase of 550% of the yield stress, and a slight increase of 27% of the Young's modulus of the coating, making it much harder and stiffer, thus fully playing its protective role. These increases can be distinguished in Fig. 7b and c by comparing simulated $P - h$ curves with the obtained parameters for as-coated (black curve) and heat-treated alumina film. The increase of the yield stress is associated to a decrease of the hardening modulus which is in accordance with a more brittle behaviour associated with the transition from amorphous to monoclinic phase shown in Appendix. Also, this crystallization could explain the slight gap between experimental and simulated $P - h$ curves for the 900°C and 1000°C heat treatment, mostly distinguishable for the cube corner test, as this phenomenon is not considered in the FEM. It should be noted that the material parameters obtained for the two heat treatments are nearly the same, which is concordant in view of the nearly similar load-displacement curves obtained for the three temperatures. It also validates yet again the robustness of the identification method in terms of unicity and stability of the inverse problem solution.

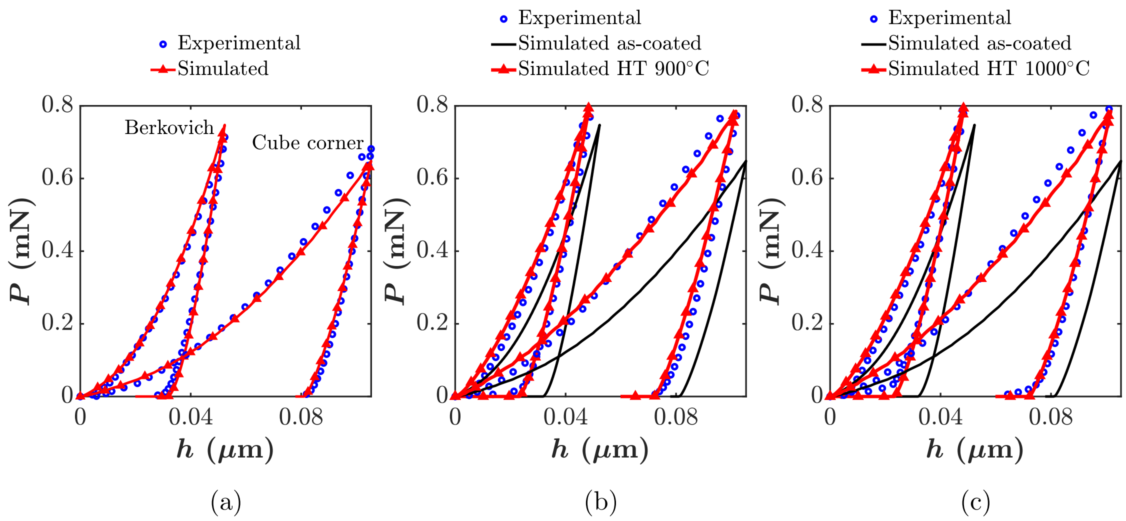

Fig. 7. Experimental and simulated $P - h$ curves obtained after identification. (**a**) Results for as-coated sample, (**b**) for heat treated samples at 900°C and (**c**) 1000°C. The simulated $P - h$ curve after identification for the as-coated sample is reported in (b) and (c).

	E (GPa)	σ_y (GPa)	H (GPa)
Behaviour	Elasticity	Plasticity	
Si substrate	173 (fixed)	6.4	0 (fixed)
Al_2O_3 as deposited	211	2.0	22
Al_2O_3 with HT	268	13.0	16

Table 2. Material parameters values of the film and the substrate identified from the inverse procedure proposed by Fauvel *et al.* [38] .The material values for the heat-treated samples are also shown here.

4.3. On the difference in elastic modulus values estimated analytically and numerically

Elastic properties of the film have been estimated using both numerical and analytical methods. However, the difference between the obtained values of elastic modulus E_f is non-negligible, notably for the as-coated sample, as shown in Table 3.

The analytical method consists in fitting CSM experimental curves according to Equation (3) and (4) by adjusting M_f and ϕ. The variation of these variables mainly influences the beginning of the curve, *i.e.* before the asymptotic behavior (Fig. 6). Experimental uncertainties prevail in the first 25 nm of penetration depth, as mentioned in section 4.1, caused by surface roughness, CSM control, as well as tip bluntness which is not taken into account in this method. Hence, these factors can explain the underestimation of the modulus value compared to the one estimated from the numerical method.

Moreover, CSM control can generate significant errors in the measured properties, as evidenced by Pharr *et al.* [62], especially for materials with high modulus-to-hardness ratios. Considering elastic modulus and initial yield stress values estimated from the numerical method (Table 2), which have been shown to be the most reliable, the as-coated film exhibits $E/\sigma_y = 106$ against $E/\sigma_y = 21$ after heat-treatment. Therefore, errors induced by CSM control greatly influence the estimated elastic modulus of as-coated film in comparison with the one of heat-treated film, which may explain the lower difference between analytical and numerical modulus values for heat-treated samples. In sum, such kind of analytical model for the estimation of elastic properties of thin films should be used carefully.

	Analytical		Numerical	$\frac{\Delta E_f}{E_f^{num}}$
	M_f (GPa)	E_f (GPa)	E_f (GPa)	
Al_2O_3 as deposited	160	146	211	31%
Al_2O_3 with HT	264	240	268	10%

Table 3. Overview of elastic modulus values of as coated and heat-treated film E_f identified using the analytical and numerical method. Analytical E_f is determined from M_f according to equation (3).

5. Single nanostructure microcompression

In this section, the identified elasto-plastic properties of the alumina coating have been integrated in 2D and 3D FEM of single nanostructure microcompression tests. Firstly, experimental tests are conducted, requiring to wisely choose tests which solicitate an individual structure. Thereafter, 2D and 3D simulation responses are confronted to experimental data, which led to an inverse analysis of the microcompression test through FEMU method in order to estimate two uncertain geometrical parameters of nanostructures.

5.1. Choice of the test

Deforming micropillars is now a classical way to apprehend the mechanical behaviour of small structures [66–68]. However, micropillars are generally obtained by FIB micromanufacturing which allows to produce samples with a controlled shape and above all, a shape in adequation with the load cell used to deform it. In the case of a nanostructure, as the one studied here, the study of the collective behaviour is generally preferred due to the very low stiffness of a single structure [69]. One of the objectives of this work is to reach the behaviour of a single structure. Fig. 8 presents a microcompression test network observed by optical microscopy. A seven-by-seven network is performed. The damaged zones are clearly distinguished. Due to misorientation and path difference between the network and the gridded nanostructure, the indenter is positioned differently relatively to the pillar for each experimental test. It means that each test is different from the others. A selection has been made to consider only those for which a pillar is loaded individually. An example of this selection is shown on Fig. 8 where SEM images of three damaged pillars loaded individually are shown. The two main criteria to discriminate such test are that the corresponding affected zone appears to be less damaged compared to the others and, above all, the flattening part of the pillar is clearly distinguished by an increase of the reflected light.

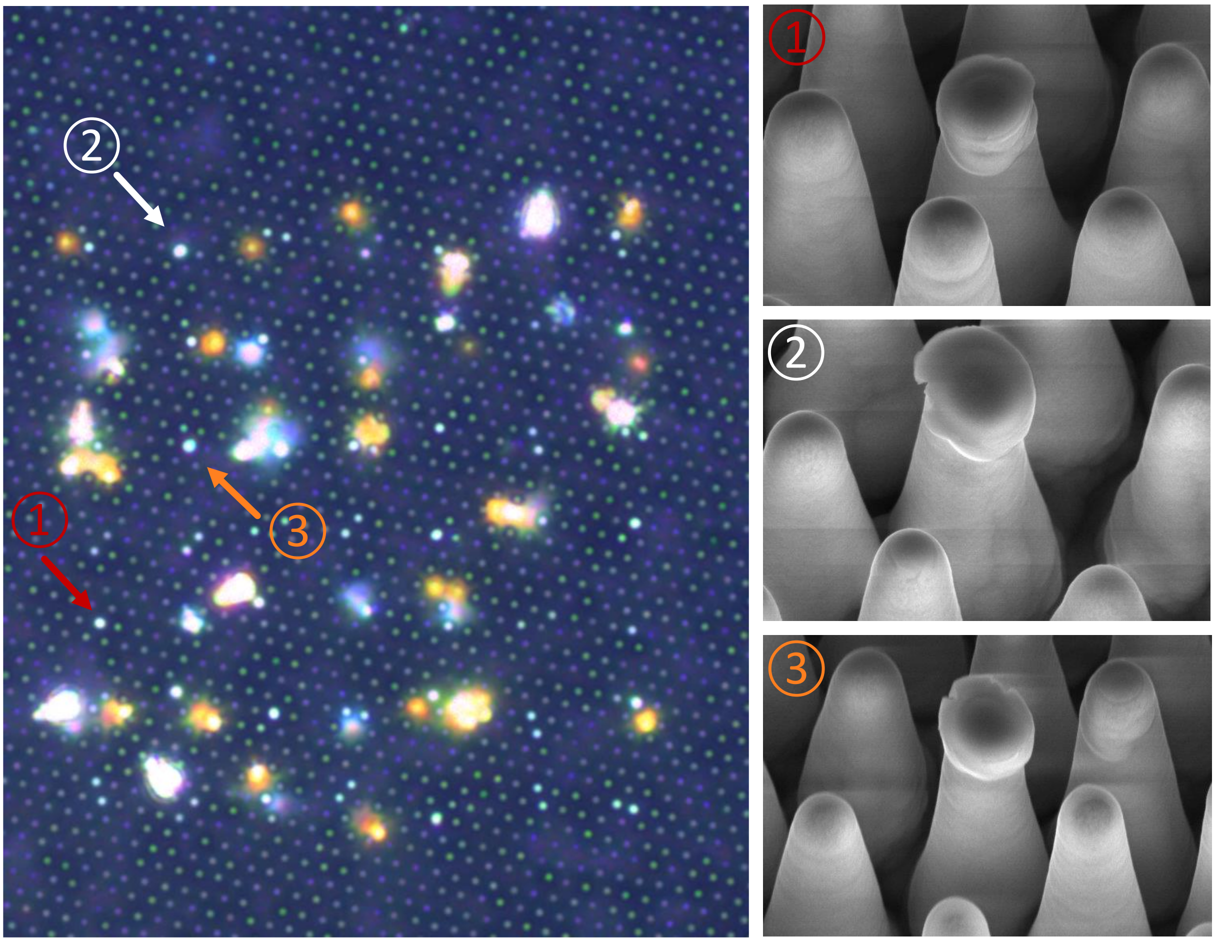

Fig. 8. Optical images of around 7 by 7 indentation network obtained with a truncated conical indenter on a coated nanostructured sample. Three microcompression tests corresponding to nanostructures loaded individually and observed by SEM are also shown. No scale is provided for confidentiality reasons.

5.2. Experimental load-displacement responses

Fig. 9 presents the typical load-displacement curve obtained for the three indentations performed at the top of a pillar chosen among the previously shown indentation network. Three stages of deformation can be distinguished for each indentation. None of them are purely elastic as the partial loading-unloading segments are never superimposed. Indeed, the first regime (stage 1) corresponds to an elasto-plastic behaviour, then a softening is observed during the second regime (stage 2) and finally a stiffening mechanism occurs in the third one (stage 3). It is also noteworthy that hysteresis phenomena on the unloading-reloading segments are observed during this last stage, particularly for the first indentation. It can be also observed that the three load-displacement curves are in the same order of magnitude, showing that the individual loading of a nanostructure is reproducible from a nanostructure to another. Only the initiation of stage 3 appears to vary. As a comparison, the typical load-displacement obtained on an uncoated Si nanostructure is also shown on Fig. 9. This is an excellent illustration of the protective effect brought by the alumina coating.

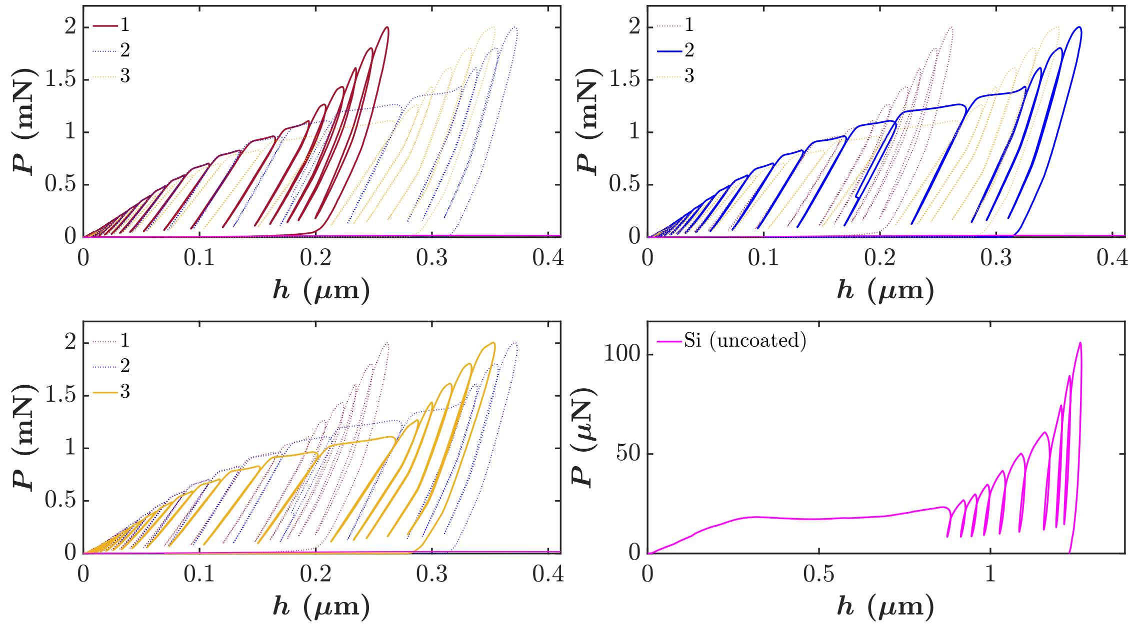

Fig. 9. Load-displacement curves obtained on the 3 coated pillars loaded individually. 3 solicitation regimes can be distinguished on each curve, which emphasize different mechanical phenomena during the microcompression test. As a comparison, the response of an uncoated pillar is also shown (magenta curve).

5.3. Simulation of microcompression tests

In order to correlate the different stages of deformation observed experimentally with the deformation behaviours suffered by the different materials composing the coated nanostructure, such nanostructure have been modelled and indented numerically. Fig. 10a shows a first comparison between the experimental response (indent number 2), and the simulated responses obtained in 2D and 3D with the material parameters listed in Table 2. All cycles are not simulated to reduce the computation time. These simulated responses are obtained with $h_{cone} =$ 2.5 µm and $r = 50$ nm, values estimated from geometrical dimensions on the SEM image in Fig. 1d. For the 3D model, seven nanostructures organised following a hexagonal shape are considered, the central nanostructure being compressed. Experimental and numerical curves appear to be similar. In particular, stage 1 and 2 can be clearly distinguished in both numerical models while stage 3 is only observed for the 3D model, suggesting that this third stage is due to the deformation of the surrounding nanostructures.

Analysing the plastic deformation field obtained on the 2D model for stage 1 and 2, as shown on Fig. 10b, it is clear that the first stage corresponds to the elasto-plastic behaviour of the layer associated with an elastic behaviour of the substrate. The second stage is reached when plastic deformation occurs in the substrate. It yields to a softening of the contact. Analysing the displacement field obtained on the 3D model (Fig. 11b orientation 0°), the third stage clearly corresponds to the contact of the indenter tip with the adjacent columns. In particular, the hysteresis caused by the friction between indenter and adjacent column [70] and the hardening are well reproduced numerically.

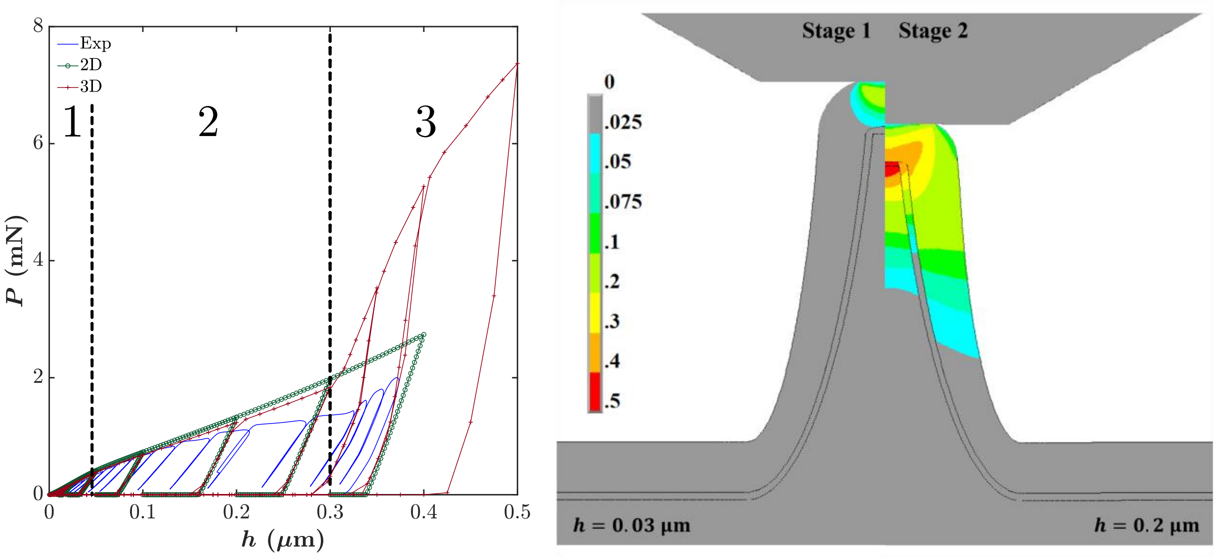

(a) (b)

Fig. 10. Confrontation of experimental (Exp) and numerical results of a nanoindentation test using a flat-ended conical indenter with 2D axisymmetric and 3D FEM. (**a**) Load-displacement curves and (**b**) plastic deformation field obtained on a single nanostructure at $h_{max} = 0.03$ µm and $h_{max} = 0.2$ µm.

Fig. 11 and Fig. 12 illustrate the sensitivity of the numerical 3D model (i) to the angle between the indenter and the nanostructure and (ii) to the distance between the indentation and the central nanostructure axis. Both parameters seem to influence above all the initiation of stage 3. Stage 1 and 2 do not seem to be modified even when inclining the indenter (or the sample) with an angle of 10°. Concerning the distance between the indentation and the nanostructure axes, a significant influence is observed only when two adjacent nanostructures are initially indented. Indeed, as long as the initial contact between the indenter and the nanostructure involves the rounded part of the nanostructure and the flat part of the indenter, the 2D model seems to be sufficient to describe the experimental behaviour. It validates the use of a 2D model as long as a single nanostructure is involved mechanically.

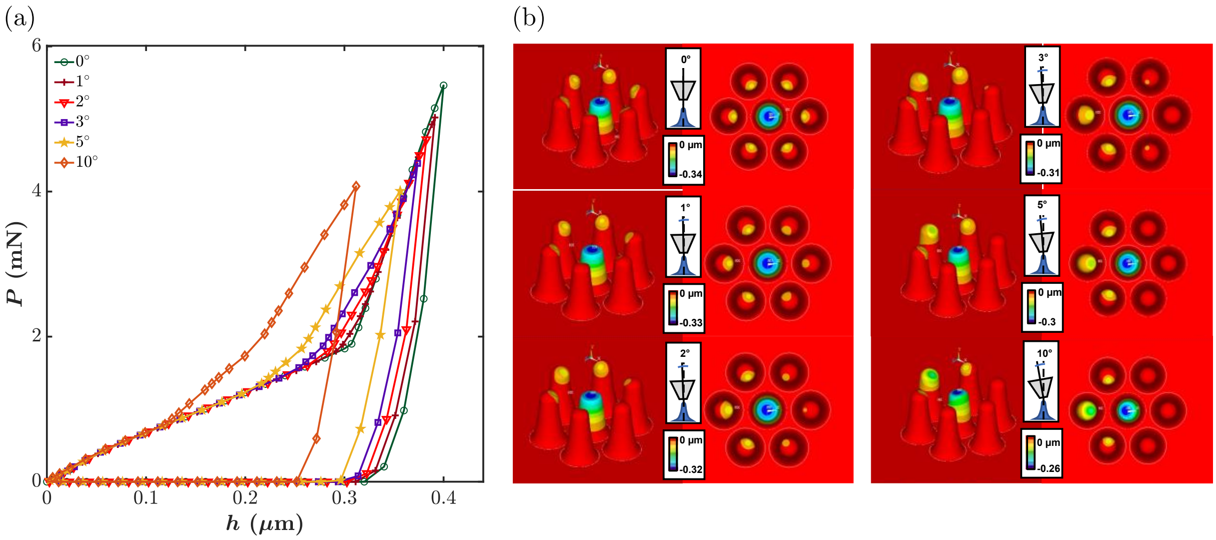

Fig. 11. Load-displacement responses on a single nanostructure and its six neighbours obtained for different orientation of the conical truncated indenter. (**a**) Load-displacement curves and (**b**) corresponding deformed nanostructures. The scale bar represents the vertical displacement.

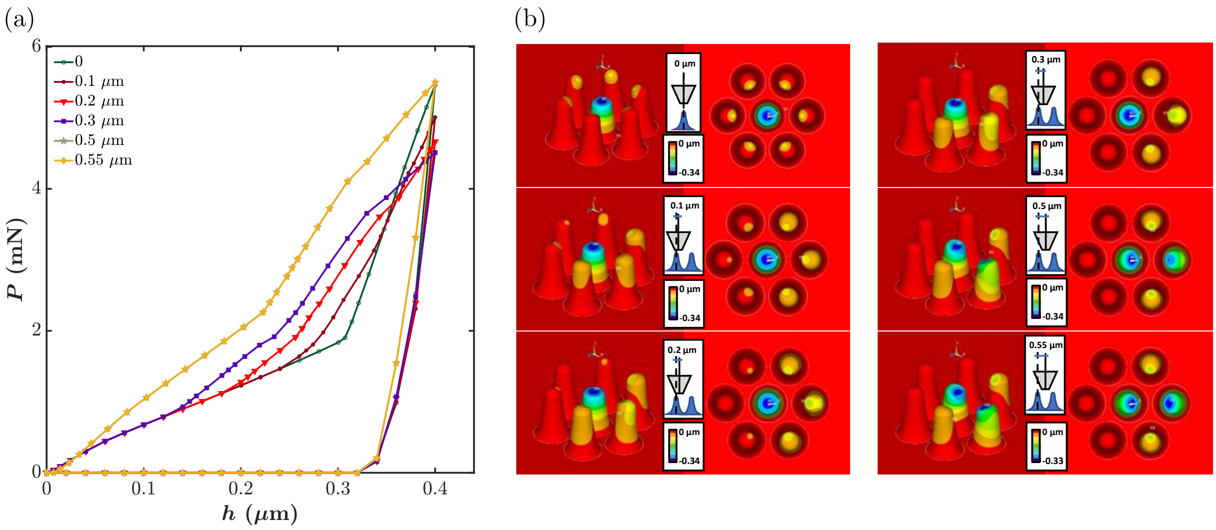

Fig. 12. Load-displacement responses on a single nanostructure and its six neighbours obtained for different location of the conical truncated indenter. (**a**) Load-displacement

curves and (**b**) corresponding deformed nanostructures. The scale bar represents the vertical displacement.

5.4. Determination of the geometric parameters of nanocones from microcompression test

If the $P-h$ curves on Fig. 10 indicate that simulation and experiment are in the same order of magnitude, they are not superimposed. Supposing that the elasto-plastic material parameters determined by the FEMU method on nanoindentation tests are true, the adjustment between experimental and simulated $P-h$ curves should lie on other structural parameters. As mentioned in section 5.1, the dimensions, and particularly the truncation radius and height (Fig. 1 and Fig. 3), are different for each pillar, making each test unique. A comparison of models and experiments seems complicated without any microstructural investigation of a given tested pillar. Thus, a tested micropillar has been examined and measured by SEM after FIB sectioning (Fig. 13a). This pillar exhibits a residual deformed height of 2.1 µm and a residual deformed truncated radius of 45 nm.

Regarding the corresponding load-displacement curve (indent 2), an inverse analysis has been performed on the first two stages using the 2D axisymmetric model, before the beginning of stage 3 which involves the surrounding structures. This analysis using the FEMU method is focused on the identification of two structural parameters, h_{cone} and r, *i.e.* the nanostructure height and its truncation radius before deformation. Fig. 13b illustrates the good correspondence between experimental (blue curve) and simulated data (red curve). The associated I-index used in [38] is 1.1, indicating a very good conditioning of the inverse problem. Associated with the fact that a single solution is encountered whatever the starting point used in the FEMU method, this solution ($h_{cone} = 4.1$ µm and $r = 41$ nm before the deformation of the covered cone) can be considered as unique and not sensitive to $P-h$ curve uncertainties. It is interesting to note that the sensitivity of the force collected by simulation to the material parameters of the film and the substrate E, σ_y, H, σ_{ys}, and to the geometrical parameters of the compressed cone, r and h_{cone}, are of the same order of magnitude. Most importantly, the simultaneous identification of six parameters (E, σ_y, H, σ_{ys}, r, h_{cone}) in a single FEMU procedure using the three tests (dual nanoindentation and microcompression) would generate an unstable solution (I >3). This reinforces the way to proceed in order to obtain parameter values with confidence, firstly the identification of material parameters by indentation and secondly, the identification of geometrical parameters by microcompression.

These structural parameters before deformation being clearly identified, they are introduced in the numerical model to perform a calculation until the maximum displacement is reached experimentally (yellow curve in Fig. 13). Then, the residual and deformed structure can be measured from this ultimate calculation. It gives, after deformation, a truncation radius of 52 nm and a residual height of 2.5 µm, which is in good accordance with the one observed by FIB (45 nm and 2.1 µm).

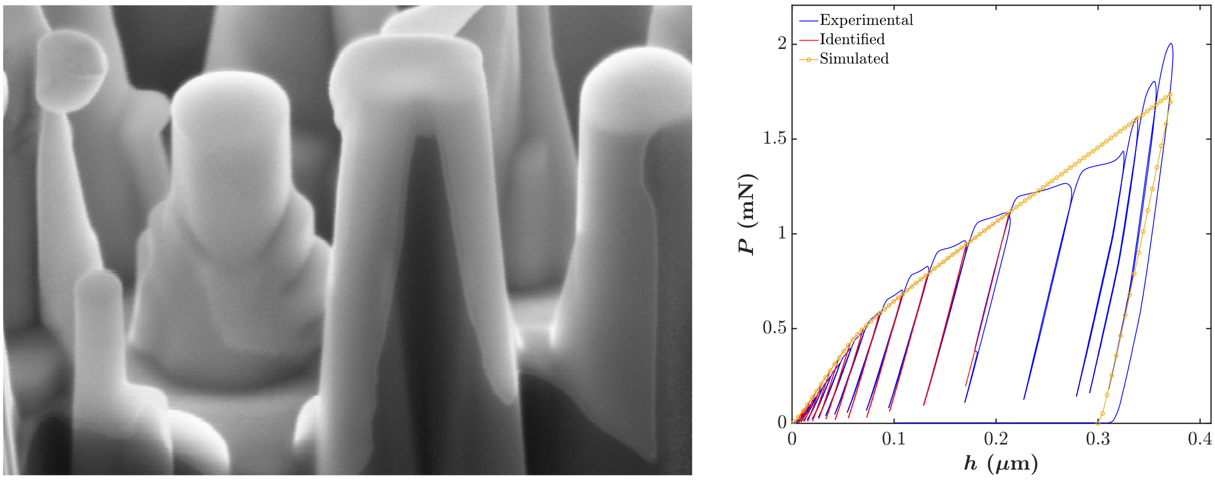

(a) (b)

Fig. 13. Confrontation of experimental and numerical observables after the microcompression test on pillar 2. (**a**) FIB cross section observed by SEM performed around test 2 (Fig. 8). (**b**) Corresponding experimental $P-h$ curve (blue), superposed with the one obtained by identification of h_{cone} and r on the first two stages (red), and with the one simulated until the maximum penetration depth is reached (yellow). No scale is provided for confidentiality reasons.

Conclusions

The deposition of an alumina thin film was found to be a suitable solution to protect nanostructured silicon optical windows. Indeed, the coating perfectly overlays the complicated shape of the substrate. Heat-treated at high temperature, this alumina layer suffers a phase transformation from an amorphous to a monoclinic phase, and its thickness remains uniform on the whole nanostructured sample.

Instrumented indentation tests on a coated planar Si substrate showed that a heat-treated Al_2O_3 film is stiffer and harder than an as-coated sample. A deeper analysis through a FEMU method supported by a design of nanoindentation experiments based on *a priori* identifiability has allowed to extract reliably both the Young's modulus, the yield stress and the hardening modulus of the layer before and after heat-treatment. The annealing of the film is indeed associated with an increase of the Young's modulus (about 27%), an increase of the yield stress (about 550%) and a decrease of the hardening modulus (about 27%), which is in total accordance with a more brittle behaviour associated with a crystallization.

The reliable identification of the elasto-plastic properties of the film have led to experiments and simulations of the mechanical behaviour of the covered nanostructures by microcompression tests. The confrontation of load displacement curves of coated and uncoated nanostructure showed that the presence of the film undeniably improves its mechanical response when solicited in microcompression. Adequate reproduction of the experimental observations on a coated nanostructure has been achieved through 2D and 3D finite element simulations, however with some non-negligible deviation from the experimental $P - h$ curve certainly due to the ignorance of geometrical dimensions of the tested nanostructures. Hence, a numerical and experimental crossed analysis has allowed to estimate by an inverse method these morphological parameters which are otherwise very difficult or even impossible to measure using experimental devices.

Finally, knowing the morphological parameters of a single nanostructure, its mechanical response can be reproduced with confidence using the material parameters determined by the FEMU method following the methodology proposed in [38]. Thus, well-designed nanoindentation experiments appear to be sufficient, relevant, and simpler to identify reliable material parameters that can be introduced in a FEM with confidence. This work paves the way of reliable 3D simulations of realistic operational conditions for such optical windows aimed to military applications, such as impact or abrasion tests.

Acknowledgements

This work has been funded by the French National Research Agency (ANR) & DGA Defense Innovation Agency (AID).

Appendix. X-ray diffraction and densification: effect of annealed temperature

From its initial amorphous phase, the as deposited Al_2O_3 is known to crystallise in its sapphire phase for temperatures up to 1000°C [42,43]. Indeed, 100 nm thick layered samples with and without nanostructures have been submitted to different heat treatments (HT), respectively at 900, 1000 and 1100°C for 90 seconds. A supplementary heat treatment at 1100°C for 1 hour has been also realised. X-rays diffraction (XRD) measurements has been performed on non-nanostructured samples after each heat treatments. XRD has been realised using a Malvern Panalytical Empyrean diffractometer.

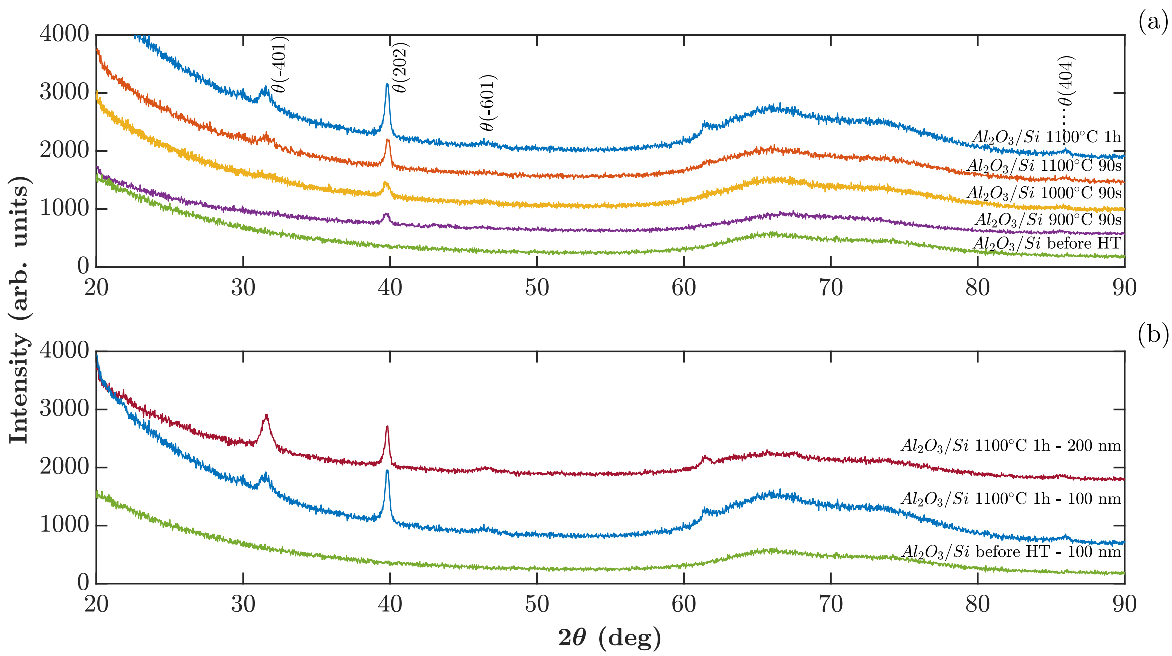

Fig. 14. XRD spectra obtained on a 100 nm thick Al_2O_3 layered silicon substrate without nanostructures. (**a**) Effect of temperature and annealing time on Al_2O_3 crystallization. (**b**) Effect of the coating thickness on Al_2O_3 crystallization.

XRD results show that the amorphous ALD Al_2O_3 layer crystallises with temperature. Fig. 14a shows that the crystallisation is all the more important as the temperature is high and the holding time is long. However only the transition from amorphous to monoclinic phase is observed. The transition from monoclinic to trigonal (sapphire) structure has not been observed in this study. This phenomenon is generally attributed to an insufficient thickness [44–46]. In this aim, the thickness of the layer has been doubled. Fig. 14b presents a comparison between the XRD spectra obtained after a heat treatment of 1 hour at 1100°C on a 100 nm thick layered sample and a 200 nm thick layered sample. As it has been already observed elsewhere [44], the increase of the thickness contributes to a better crystallisation of the sample. However, once again, the trigonal phase is not observed.

References

[1] J. Yong, Q. Yang, J. Huo, X. Hou, F. Chen, Underwater gas self-transportation along femtosecond laser-written open superhydrophobic surface microchannels (<100 µm) for bubble/gas manipulation, Int. J. Extreme Manuf. 4 (2022) 015002. https://doi.org/10.1088/2631-7990/ac466f.

[2] I. Ielo, F. Giacobello, S. Sfameni, G. Rando, M. Galletta, V. Trovato, G. Rosace, M.R. Plutino, Nanostructured Surface Finishing and Coatings: Functional Properties and Applications, Materials. 14 (2021) 2733. https://doi.org/10.3390/ma14112733.

[3] S. Salaluk, S. Jiang, E. Viyanit, M. Rohwerder, K. Landfester, D. Crespy, Design of Nanostructured Protective Coatings with a Sensing Function, ACS Appl. Mater. Interfaces. 13 (2021) 53046–53054. https://doi.org/10.1021/acsami.1c14110.

[4] H. Wang, Z. Zhang, J. Zheng, J. Zhao, Y. Liang, X. Li, L. Ren, Multifunctional superhydrophobic surface with dynamically controllable micro/nanostructures for droplet manipulation and friction control, Chem. Eng. J. 417 (2021) 127944. https://doi.org/10.1016/j.cej.2020.127944.

[5] A. Al Hossain, M. Yang, A. Checco, G. Doerk, C.E. Colosqui, Large-area nanostructured surfaces with tunable zeta potentials, Appl. Mater. Today. 19 (2020) 100553. https://doi.org/10.1016/j.apmt.2019.100553.

[6] Q. Wang, A. Samanta, S.K. Shaw, H. Hu, H. Ding, Nanosecond laser-based high-throughput surface nanostructuring (nHSN), Appl. Surf. Sci. 507 (2020) 145136. https://doi.org/10.1016/j.apsusc.2019.145136.

[7] J. Song, D. Wang, L. Hu, X. Huang, Y. Chen, Superhydrophobic surface fabricated by nanosecond laser and perhydropolysilazane, Appl. Surf. Sci. 455 (2018) 771–779. https://doi.org/10.1016/j.apsusc.2018.05.227.

[8] X. Gao, X. Yan, X. Yao, L. Xu, K. Zhang, J. Zhang, B. Yang, L. Jiang, The Dry-Style Antifogging Properties of Mosquito Compound Eyes and Artificial Analogues Prepared by Soft Lithography, Adv. Mater. 19 (2007) 2213–2217. https://doi.org/10.1002/adma.200601946.

[9] T. Mouterde, G. Lehoucq, S. Xavier, A. Checco, C.T. Black, A. Rahman, T. Midavaine, C. Clanet, D. Quéré, Antifogging abilities of model nanotextures, Nat. Mater. 16 (2017) 658–663. https://doi.org/10.1038/nmat4868.

[10] M. Banik, P. Chakrabarty, A. Das, S.K. Ray, R. Mukherjee, Colloidal Transfer Printing–Mediated Fabrication of Zinc Oxide Nanorods for Self-Cleaning Applications, Adv. Mater. Interfaces. 6 (2019) 1900063. https://doi.org/10.1002/admi.201900063.

[11] S.M. Varughese, N. Bhandaru, Durability of submerged hydrophobic surfaces, Soft Matter. 16 (2020) 1692–1701. https://doi.org/10.1039/C9SM01942A.

[12] U.U. Ghosh, S. Nair, A. Das, R. Mukherjee, S. DasGupta, Replicating and resolving wetting and adhesion characteristics of a Rose petal, Colloids Surf. Physicochem. Eng. Asp. 561 (2019) 9–17. https://doi.org/10.1016/j.colsurfa.2018.10.028.

[13] D.G. Stavenga, S. Foletti, G. Palasantzas, K. Arikawa, Light on the moth-eye corneal nipple array of butterflies, Proc. R. Soc. B Biol. Sci. 273 (2006) 661–667. https://doi.org/10.1098/rspb.2005.3369.
[14] S.J. Wilson, M.C. Hutley, The Optical Properties of "Moth Eye" Antireflection Surfaces, Opt. Acta Int. J. Opt. 29 (1982) 993–1009. https://doi.org/10.1080/713820946.
[15] M. Arias, J. Mappes, C. Desbois, S. Gordon, M. McClure, M. Elias, O. Nokelainen, D. Gomez, Transparency reduces predator detection in mimetic clearwing butterflies, Funct. Ecol. 33 (2019) 1110–1119. https://doi.org/10.1111/1365-2435.13315.
[16] R.H. Siddique, G. Gomard, H. Hölscher, The role of random nanostructures for the omnidirectional anti-reflection properties of the glasswing butterfly, Nat. Commun. 6 (2015) 6909. https://doi.org/10.1038/ncomms7909.
[17] A. Yoshida, M. Motoyama, A. Kosaku, K. Miyamoto, Antireflective Nanoprotuberance Array in the Transparent Wing of a Hawkmoth, Cephonodes hylas, Zoolog. Sci. 14 (1997) 737–741. https://doi.org/10.2108/zsj.14.737.
[18] A. Yoshida, M. Motoyama, A. Kosaku, K. Miyamoto, Nanoprotuberance Array in the Transparent Wing of a Hawkmoth, Cephonodes hylas, Zoolog. Sci. 13 (1996) 525–526. https://doi.org/10.2108/zsj.13.525.
[19] P. Lecointre, T. Mouterde, A. Checco, C.T. Black, A. Rahman, C. Clanet, D. Quéré, Ballistics of self-jumping microdroplets, Phys. Rev. Fluids. 4 (2019) 013601. https://doi.org/10.1103/PhysRevFluids.4.013601.
[20] K.M. Wisdom, J.A. Watson, X. Qu, F. Liu, G.S. Watson, C.-H. Chen, Self-cleaning of superhydrophobic surfaces by self-propelled jumping condensate, Proc. Natl. Acad. Sci. 110 (2013) 7992–7997. https://doi.org/10.1073/pnas.1210770110.
[21] D.A. Boyd, J.A. Frantz, R. Nimalan, L.E. Busse, W. Kim, S.S. Bayya, J.S. Sanghera, Periodically patterned germanium surfaces modified to form superhydrophobic, IR-transmissive substrates, Opt. Mater. Express. 6 (2016) 3254. https://doi.org/10.1364/OME.6.003254.
[22] J.W. Leem, Y. Yeh, J.S. Yu, Enhanced transmittance and hydrophilicity of nanostructured glass substrates with antireflective properties using disordered gold nanopatterns, Opt. Express. 20 (2012) 4056. https://doi.org/10.1364/OE.20.004056.
[23] K.-C. Park, H.J. Choi, C.-H. Chang, R.E. Cohen, G.H. McKinley, G. Barbastathis, Nanotextured Silica Surfaces with Robust Superhydrophobicity and Omnidirectional Broadband Supertransmissivity, ACS Nano. 6 (2012) 3789–3799. https://doi.org/10.1021/nn301112t.
[24] W.-L. Min, B. Jiang, P. Jiang, Bioinspired Self-Cleaning Antireflection Coatings, Adv. Mater. 20 (2008) 3914–3918. https://doi.org/10.1002/adma.200800791.
[25] F. Xia, L. Jiang, Bio-Inspired, Smart, Multiscale Interfacial Materials, Adv. Mater. 20 (2008) 2842–2858. https://doi.org/10.1002/adma.200800836.
[26] J.-G. Kim, H.J. Choi, K.-C. Park, R.E. Cohen, G.H. McKinley, G. Barbastathis, Multifunctional Inverted Nanocone Arrays for Non-Wetting, Self-Cleaning Transparent Surface with High Mechanical Robustness, Small. 10 (2014) 2487–2494. https://doi.org/10.1002/smll.201303051.
[27] U. Mehmood, F.A. Al-Sulaiman, B.S. Yilbas, B. Salhi, S.H.A. Ahmed, M.K. Hossain, Superhydrophobic surfaces with antireflection properties for solar applications: A critical review, Sol. Energy Mater. Sol. Cells. 157 (2016) 604–623. https://doi.org/10.1016/j.solmat.2016.07.038.
[28] T. Mouterde, Matériaux multifonctions : antipluie, antibuée, antireflets, 2017. http://www.theses.fr/2017SACLX015/document.

[29] P. Lecointre, Texture-induced hydrophobicity, and some collective effects in granular matter and economics, Theses, Institut Polytechnique de Paris, 2019. https://tel.archives-ouvertes.fr/tel-03092267.
[30] P. Lecointre, S. Laney, M. Michalska, T. Li, A. Tanguy, I. Papakonstantinou, D. Quéré, Unique and universal dew-repellency of nanocones, Nat. Commun. 12 (2021) 3458. https://doi.org/10.1038/s41467-021-23708-6.
[31] E. Nyankson, H. Agbe, G.K.S. Takyi, Y.D. Bensah, D.K. Sarkar, Recent advances in nanostructured superhydrophobic surfaces: fabrication and long-term durability challenges, Curr. Opin. Chem. Eng. 36 (2022) 100790. https://doi.org/10.1016/j.coche.2021.100790.
[32] Y. Chen, J. Zhang, High-Speed Erosion Behavior of Hydrophobic Micro/Nanostructured Titanium Surfaces, Nanomaterials. 12 (2022) 880. https://doi.org/10.3390/nano12050880.
[33] D.S. Hobbs, B.D. MacLeod, R.J. Ondercin, Initial Erosion Studies of Microstructure-Based Anti-Reflection Treatments in Zinc Sulfide, in: 2008: pp. 1–18.
[34] D.S. Hobbs, Study of the environmental and optical durability of AR microstructures in sapphire, ALON, and diamond, in: R.W. Tustison (Ed.), Orlando, Florida, USA, 2009: p. 73020J. https://doi.org/10.1117/12.818335.
[35] A. K., A. Varade, N.R. K., S. Dhan, C. M., B. N., P. Krishna, Synthesis of high hardness IR optical coating using diamond-like carbon by PECVD at room temperature, Diam. Relat. Mater. 78 (2017) 39–43. https://doi.org/10.1016/j.diamond.2017.07.008.
[36] A.S. Grenadyorov, A.A. Solovyev, K.V. Oskomov, V.O. Oskirko, V.A. Semenov, Thermal stability of anti-reflective and protective a-C:H:SiOx coating for infrared optics, Appl. Surf. Sci. 510 (2020) 145433. https://doi.org/10.1016/j.apsusc.2020.145433.
[37] R. Aubry, G. Lehoucq, R. Guillemet, J. Cholet, J.-P. Martins, M.-S.-L. Lee Bouhours, A. Delboulbe, Optical transmission element, having a super-hydrophobic nanostructured surface having an anti-reflective property and covered with a compliant high-density thin film deposit, WO2020178304, 2020. https://worldwide.espacenet.com/publicationDetails/biblio?II=0&ND=3&adjacent=true&locale=fr_EP&FT=D&date=20200910&CC=WO&NR=2020178304A1&KC=A1#.
[38] V. Fauvel, Y. Gaillard, R. Guillemet, P. Garabédian, F. Richard, Simultaneous extraction of the elastic-plastic properties of a thin film and its substrate from an identifiability-based design of depth-sensing nanoindentation testing, J. Mech. Phys. Solids. 163 (2022) 104860. https://doi.org/10.1016/j.jmps.2022.104860.
[39] V. Fauvel, Élaboration et caractérisation mécanique par nanoindentation de fenêtres optiques nanostructurées superhydrophobes et antireflets, Theses, Université Bourgogne Franche-Comté, 2022. https://tel.archives-ouvertes.fr/tel-03828063.
[40] E. Beche, F. Fournel, V. Larrey, F. Rieutord, C. Morales, A.-M. Charvet, F. Madeira, G. Audoit, J.-M. Fabbri, Direct Bonding Mechanism of ALD-Al2O3 Thin Films, ECS J. Solid State Sci. Technol. 4 (2015) P171–P175. https://doi.org/10.1149/2.0241505jss.
[41] J.N. Ding, X.F. Wang, N.Y. Yuan, C.L. Li, Y.Y. Zhu, B. Kan, The influence of substrate on the adhesion behaviors of atomic layer deposited aluminum oxide films, Surf. Coat. Technol. 205 (2011) 2846–2851. https://doi.org/10.1016/j.surfcoat.2010.10.052.
[42] A. Boumaza, L. Favaro, J. Lédion, G. Sattonnay, J.B. Brubach, P. Berthet, A.M. Huntz, P. Roy, R. Tétot, Transition alumina phases induced by heat treatment of boehmite: An X-ray diffraction and infrared spectroscopy study, J. Solid State Chem. 182 (2009) 1171–1176. https://doi.org/10.1016/j.jssc.2009.02.006.
[43] P.S. Santos, H.S. Santos, S.P. Toledo, Standard transition aluminas. Electron microscopy studies, Mater. Res. 3 (2000) 104–114. https://doi.org/10.1590/S1516-14392000000400003.

[44] J. Musil, J. Blažek, P. Zeman, Š. Prokšová, M. Šašek, R. Čerstvý, Thermal stability of alumina thin films containing γ-Al2O3 phase prepared by reactive magnetron sputtering, Appl. Surf. Sci. 257 (2010) 1058–1062. https://doi.org/10.1016/j.apsusc.2010.07.107.
[45] P. Nayar, A. Khanna, Formation of crystalline aluminum silicate hydroxide layer during deposition of amorphous alumina coatings by electron beam evaporation, Vacuum. 89 (2013) 17–20. https://doi.org/10.1016/j.vacuum.2012.08.015.
[46] P. Nayar, A. Khanna, D. Kabiraj, S.R. Abhilash, B.D. Beake, Y. Losset, B. Chen, Structural, optical and mechanical properties of amorphous and crystalline alumina thin films, Thin Solid Films. 568 (2014) 19–24. https://doi.org/10.1016/j.tsf.2014.07.053.
[47] W.C. Oliver, G.M. Pharr, An improved technique for determining hardness and elastic modulus using load and displacement sensing indentation experiments, J. Mater. Res. 7 (1992) 1564–1583. https://doi.org/10.1557/JMR.1992.1564.
[48] J.B. Pethica, W.C. Oliver, Mechanical Properties of Nanometre Volumes of Material: use of the Elastic Response of Small Area Indentations, MRS Proc. 130 (1988) 13. https://doi.org/10.1557/PROC-130-13.
[49] G.M. Pharr, W.C. Oliver, Measurement of Thin Film Mechanical Properties Using Nanoindentation, MRS Bull. 17 (1992) 28–33. https://doi.org/10.1557/S0883769400041634.
[50] M.C. Barick, Y. Gaillard, A. Lejeune, F. Amiot, F. Richard, On the uniqueness of intrinsic viscoelastic properties of materials extracted from nanoindentation using FEMU, Int. J. Solids Struct. 202 (2020) 929–946. https://doi.org/10.1016/j.ijsolstr.2020.03.015.
[51] R.B. King, Elastic analysis of some punch problems for a layered medium, Int. J. Solids Struct. 23 (1987) 1657–1664. https://doi.org/10.1016/0020-7683(87)90116-8.
[52] S. Bec, A. Tonck, J.L. Loubet, A simple guide to determine elastic properties of films on substrate from nanoindentation experiments, Philos. Mag. 86 (2006) 5347–5358. https://doi.org/10.1080/14786430600660856.
[53] H. Gao, C. Cheng-Hsin, L. Jin, Elastic contact versus indentation modeling of multi-layered materials, Int. J. Solids Struct. 29 (1992) 2471–2492. https://doi.org/10.1016/0020-7683(92)90004-D.
[54] P. Delobelle, S. Dali, F. Richard, Interprétation du module d'indentation dans le cas des matériaux anisotropes et/ou actifs, Matér. Tech. 99 (2011) 185–196. https://doi.org/10.1051/mattech/2011032.
[55] J.J. Hall, Electronic Effects in the Elastic Constants of n -Type Silicon, Phys. Rev. 161 (1967) 756–761. https://doi.org/10.1103/PhysRev.161.756.
[56] R. Hill, The Elastic Behaviour of a Crystalline Aggregate, Proc. Phys. Soc. Sect. A. 65 (1952) 349–354. https://doi.org/10.1088/0370-1298/65/5/307.
[57] G. Kermouche, E. Barthel, D. Vandembroucq, Ph. Dubujet, Mechanical modelling of indentation-induced densification in amorphous silica, Acta Mater. 56 (2008) 3222–3228. https://doi.org/10.1016/j.actamat.2008.03.010.
[58] F. Richard, M. Villars, S. Thibaud, Viscoelastic modeling and quantitative experimental characterization of normal and osteoarthritic human articular cartilage using indentation, J. Mech. Behav. Biomed. Mater. 24 (2013) 41–52. https://doi.org/10.1016/j.jmbbm.2013.04.012.
[59] M.-J. Pac, S. Giljean, C. Rousselot, F. Richard, P. Delobelle, Microstructural and elasto-plastic material parameters identification by inverse finite elements method of Ti (1−x) Al x N (0 < x < 1) sputtered thin films from Berkovich nano-indentation experiments, Thin Solid Films. 569 (2014) 81–92. https://doi.org/10.1016/j.tsf.2014.07.037.
[60] E. Renner, A. Bourceret, Y. Gaillard, F. Amiot, P. Delobelle, F. Richard, Identifiability of single crystal plasticity parameters from residual topographies in Berkovich

nanoindentation on FCC nickel, J. Mech. Phys. Solids. 138 (2020) 103916. https://doi.org/10.1016/j.jmps.2020.103916.
[61] F. Richard, MIC2M, (n.d.). http://mic2m.univ-fcomte.fr/.
[62] G.M. Pharr, J.H. Strader, W.C. Oliver, Critical issues in making small-depth mechanical property measurements by nanoindentation with continuous stiffness measurement, J. Mater. Res. 24 (2009) 653–666. https://doi.org/10.1557/jmr.2009.0096.
[63] K.W. Siu, A.H.W. Ngan, The continuous stiffness measurement technique in nanoindentation intrinsically modifies the strength of the sample, Philos. Mag. 93 (2013) 449–467. https://doi.org/10.1080/14786435.2012.722234.
[64] M. Qasmi, P. Delobelle, Influence of the average roughness Rms on the precision of the Young's modulus and hardness determination using nanoindentation technique with a Berkovich indenter, Surf. Coat. Technol. 201 (2006) 1191–1199. https://doi.org/10.1016/j.surfcoat.2006.01.058.
[65] E.O. Hall, The Deformation and Ageing of Mild Steel: II Characteristics of the L ders Deformation, Proc. Phys. Soc. Sect. B. 64 (1951) 742–747. https://doi.org/10.1088/0370-1301/64/9/302.
[66] C. Kirchlechner, J. Keckes, C. Motz, W. Grosinger, M.W. Kapp, J.S. Micha, O. Ulrich, G. Dehm, Impact of instrumental constraints and imperfections on the dislocation structure in micron-sized Cu compression pillars, Acta Mater. 59 (2011) 5618–5626. https://doi.org/10.1016/j.actamat.2011.05.037.
[67] F. Östlund, K. Rzepiejewska-Malyska, K. Leifer, L.M. Hale, Y. Tang, R. Ballarini, W.W. Gerberich, J. Michler, Brittle-to-Ductile Transition in Uniaxial Compression of Silicon Pillars at Room Temperature, Adv. Funct. Mater. 19 (2009) 2439–2444. https://doi.org/10.1002/adfm.200900418.
[68] A. Merabet, M. Texier, C. Tromas, S. Brochard, L. Pizzagalli, L. Thilly, J. Rabier, A. Talneau, Y.-M. Le Vaillant, O. Thomas, J. Godet, Low-temperature intrinsic plasticity in silicon at small scales, Acta Mater. 161 (2018) 54–60. https://doi.org/10.1016/j.actamat.2018.09.025.
[69] V. Doquet, A. Tanguy, S. Hallais, R. Guillemet, J. Cholet, D. Jussey, Mechanical behavior of surface-patterned and coated Si or Ge wafers for superhydrophobic and antireflective light transmitting windows, J. Mater. Sci. 57 (2022) 955–971. https://doi.org/10.1007/s10853-021-06794-1.
[70] Y. Gaillard, E. Jimenez-Piqué, M. Oliva-Ramirez, V.J. Rico, A.R. Gonzalez-Elipe, Extraction of microstructural parameters from sculptured thin films nanoindentation, Surf. Coat. Technol. 425 (2021) 127696. https://doi.org/10.1016/j.surfcoat.2021.127696.